Two-step transfer mechanisms in the charge-exchange reaction ^{40}Ca(^{18}O, ^{18}F)^{40}K at 275 MeV

B. Urazbekov [1,2,*] N. Burtebayev,[2] F. Cappuzzello [3,4] D. Carbone [3]
M. Cavallaro,[3] M. Colonna,[3] A. Gargano [5] and A. Spatafora [3]

(NUMEN Collaboration)

[1]*Department of Nuclear Physics and Nanotechnology, L N Gumilyov Eurasian National University,
Satpayev Str. 2, Astana 010008, Kazakhstan*
[2]*Institute of Nuclear Physics, Laboratory of Low Energy Reactions, Ibragimov Str. 1, Almaty 050032, Kazakhstan*
[3]*Istituto Nazionale di Fisica Nucleare, Laboratori Nazionali del Sud, Via S. Sofia, 62, 95123 Catania, Italy*
[4]*Dipartimento di Fisica e Astronomia "Ettore Majorana", Università di Catania, Via S. Sofia, 64, 95123 Catania, Italy*
[5]*Istituto Nazionale di Fisica Nucleare, Complesso Universitario di Monte S.Angelo, Via Cintia, I-80126 Napoli, Italy*

The nuclear collision ^{18}O $+$ ^{40}Ca at 275 MeV is theoretically studied in the elastic, inelastic, one-nucleon transfer, and charge-exchange channels. The elastic scattering channel is treated within the optical model framework with the help of semimicroscopic double folding potentials, which are constructed by using the realistic nuclear matter densities obtained within the Hartree-Fock-Bogoliubov method, while the distorted wave Born approximation method is adopted to calculate differential cross sections for the other channels. The charge exchange nuclear reaction ^{40}Ca(^{18}O, ^{18}F)^{40}K is analyzed by assuming the two-step transfer mechanisms, namely by considering a succession of proton-neutron pickup-stripping processes. Large-scale shell-model calculations are employed to compute the spectroscopic amplitudes, needed in our approach. When compared to the available experimental angular distributions, the obtained results show that the two-step transfer mechanisms play a relevant role in the description of the ^{40}Ca(^{18}O, ^{18}F)^{40}K reaction and need to be accounted for in any accurate analysis of the measured cross section.

I. INTRODUCTION

In past decades, charge-exchange reactions were performed to carry out studies on isospin structures [1–3] and isovector interactions between colliding nuclei [4–6]. Charge-exchange reactions also are a relevant tool for investigating the properties of exotic nuclei [7–9]. Recently, the particular interest in the research of charge-exchange reactions traces back to the opportunity to get information on the analog weak processes, as proposed by the NUMEN project [10–12].

In particular, the main aim of the NUMEN project is to use the heavy-ion double-charge exchange (DCE) reactions as surrogate processes to study the neutrinoless double beta ($0\nu\beta\beta$) decay and explore for possible connections between the $0\nu\beta\beta$ nuclear and DCE matrix elements. As a matter of fact, a linearly dependent correlation has been evidenced between the double Gamow-Teller DCE and $0\nu\beta\beta$ matrix elements in Refs. [13,14] within the shell-model framework. At present, the phenomenon of $0\nu\beta\beta$ decay is one of the most important trends in modern physics, its existence showing deviations from the standard model of particle physics. It is expected that a clear understanding of the nuclear matrix elements may point the way to access neutrino mass.

Within the NUMEN project, experimental work was performed to obtain a differential cross section of the ^{40}Ca(^{18}O, ^{18}Ne)^{40}Ar DCE reaction at beam energy of 275 MeV [15]. This resulted in high mass resolution, angular distribution, energy distribution and accurate cross sections at forward scattering angles, including zero degrees. In such study the experimental feasibility of the zero degree DCE measurements was proven together with the possibility of extracting nuclear matrix elements (NME) of DCE reactions adopting a schematic approach. Theoretical developments have been performed in the very last years [12,16–19]. Nowadays, the construction of a complete theory of DCE reactions, needed to microscopically extract the NME of DCE reactions, is still in progress. In this context, the theoretical study of intermediate channels and competing reaction mechanisms remains an important issue, which is particularly effective when all channels are studied under the same experimental conditions and within a unique theoretical framework [20–22]. A successful description of the single charge-exchange (SCE) reactions is needed not only to understand the full picture of these reactions but to clarify the information needed for accurate calculations of DCE cross sections [23].

The study of the ^{40}Ca(^{18}O, ^{18}F)^{40}K SCE reaction at the same incident energy and at the same experimental conditions as the DCE was carried out by some of us in Ref. [24], where the distorted wave Born approximation (DWBA) was applied with nuclear transition densities obtained by

_____
*bakytzhan.urazbekov@gmail.com

quasiparticle random phase approximation (QRPA) approach [25]. The authors could successfully explain the experimental differential cross sections of the SCE reaction but only for higher excited states of ^{40}K in the exit channels ^{18}F + ^{40}K*. It was concluded that the reason for the underestimation of the theoretical approach might be related to deficiencies in the nuclear transition densities which may require a more careful treatment of the polarization effects. It was also concluded that one more possible gap is in the competition of two-step transfer mechanisms of two nucleons, which was not taken into account in the study.

In this regard, we focus on the ^{40}Ca(^{18}O, ^{18}F) ^{40}K re-action with the main goal to determine the contribution of the mechanisms of two-step transfer. To do this, we need to start by establishing the optical potentials and the spectroscopic amplitudes that are needed in the calculations of the two-step transfer reactions. We also need to make sure that the resulting theoretical cross sections for the elastic and inelastic scattering channels match reality by comparing with the available experimental data [24]. With the aid of the obtained optical potentials and spectroscopic amplitudes, the proper theoretical description for the angular distributions of intermediate channels [26] is also important because it gives us confidence that we are moving in the right direction to an objective assessment of the individual contributions of the two-step mechanisms.

The present work is organized as follows. Section II reports the results of calculations for both elastic and inelastic channels for testing the capabilities of the optical potentials. In Sec. III, we present the resulting cross sections of the one-nucleon transfer channels, and the role of the two-step transfer mechanisms in SCE channels is discussed in Sec. IV. Finally, the major findings are drawn in Conclusions in Sec. V.

II. ELASTIC AND INELASTIC SCATTERING CHANNELS

A. Elastic channel

The angular distribution data on the elastic scattering of ^{18}O + ^{40}Ca have been analyzed within the optical model (OM) by means of the FRESCO code [21]. The OM calculations were carried out with the complex potential given by

$$U(R) = V^C(R) - V(R) - iW(R), \quad (1)$$

where $V^C(R)$ is the Coulomb potential, $V(R)$ and $W(R)$ are, respectively, the real and imaginary parts of the nuclear volume potential. The Coulomb potential may be taken as the interaction of a point-charge with a uniformly charged sphere

$$V^C(R) = \begin{cases} \frac{Z_1 Z_2 e^2}{2R_C}\left(3 - \frac{R^2}{R_C^2}\right), & \text{for } R \leqslant R_C, \\ \frac{Z_1 Z_2 e^2}{R}, & \text{for } R > R_C, \end{cases} \quad (2)$$

while real and imaginary parts can be taken as parametrized Woods-Saxon functions:

$$V(R) = V_0 \left[1 + \exp\left(\frac{R - R_v}{a_v}\right)\right]^{-1}, \quad (3)$$

$$W(R) = W_0 \left[1 + \exp\left(\frac{R - R_w}{a_w}\right)\right]^{-1}. \quad (4)$$
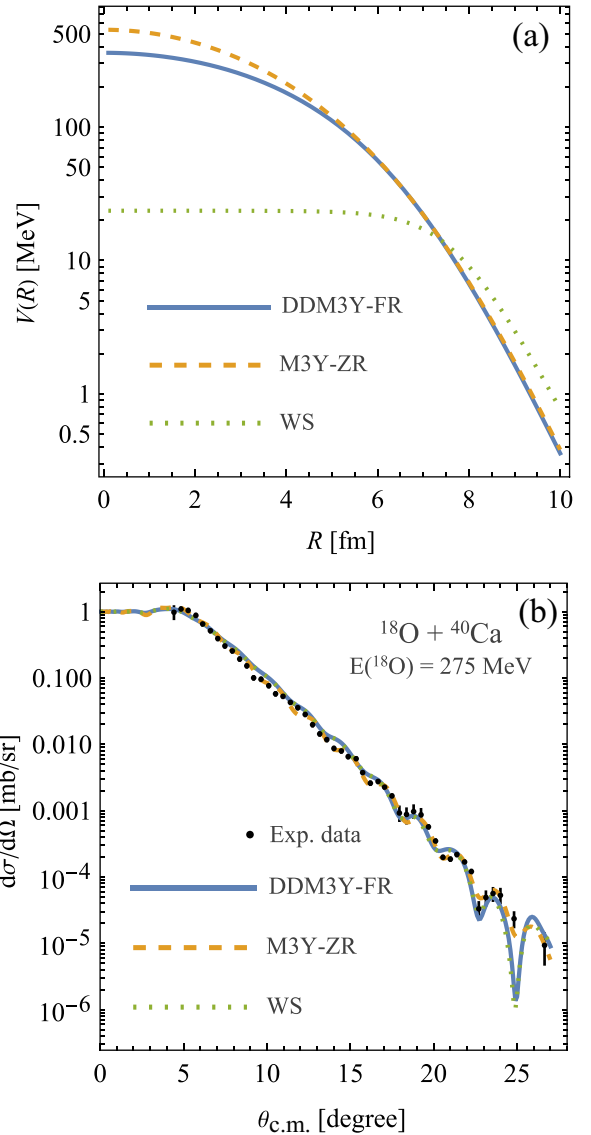
FIG. 1. (a) Real parts of the optical potentials used in the OM analysis. (b) Elastic scattering cross sections in comparison with the OM calculations for a variety of optical potentials. Experimental data are from Ref. [24].

Alternatively, the real potential $V(R)$ can also be built by means of the double folding [27] model as follows:

$$V(\mathbf{R}) \equiv N_R V^{DF}(\mathbf{R}) = \int d\mathbf{r}_1 d\mathbf{r}_2\, \rho_1(\mathbf{r}_1)$$
$$\times V_{NN}(\mathbf{R}_{NN} = \mathbf{R} - \mathbf{r}_1 + \mathbf{r}_2)\rho_2(\mathbf{r}_2), \quad (5)$$

where N_R is the normalization factor, r_i and ρ_i are the internal radii and nuclear matter density functions, respectively, potential V_{NN} stands for the nucleon-nucleon potential, and R_{NN} is the distance between them.

In this work, we have used three complex potentials for the analysis of elastic scattering: one fully based on Woods-Saxon (WS) phenomenological potentials, the other two, M3Y-ZR and DDM3Y-FR, on semimicroscopic potentials within the double folding model obtained using the interaction from

TABLE I. Optical potential parameters used in the OM calculations.

DF potential	V_0 MeV	R_v fm	a_v fm	J_{Re} MeV fm^3	$\sqrt{\langle R_v^2 \rangle}$ fm	W_0 MeV	R_w fm	a_w fm	J_{Im} MeV fm^3	$\sqrt{\langle R_w^2 \rangle}$ fm	R_C fm	σ_r mb	χ^2/N
WS	23.60	7.67	0.687	67.9	5.58	5.75	8.69	0.69	1.82	2.79	7.85	2485	2.59
M3Y-ZR	0.67[a]			266.9	4.67	67.3	6.05	1.05	112.3	6.08	7.85	2984	7.17
DDM3Y-FR	0.55[a]			230.9	4.84	147.7	5.03	1.08	159.0	5.56	7.85	2970	7.20

[a]Stands for the normalization factor N_R.

Ref. [28]. The two latter potentials differ in the calculation method of their exchange parts. In particular, the DDM3Y-FR takes into account the density dependence and knock-on exchange effects [29,30].

The double folding potentials were calculated by means of the BIFOLD PYTHON-based computer code [31]. The realistic nuclear matter densities were obtained within the Hartree-Fock-Bogoliubov (HFB) framework with the BSk2 Skyrme force [32–34].

The optical potential parameters have been adjusted to the experimental data by using the χ-square procedure, namely, by minimizing the function

$$\chi^2 = \sum_{i=1}^{N} \left(\frac{\sigma_i^{th} - \sigma_i^{\exp}}{\sigma_i^{err}} \right)^2, \quad (6)$$

where N is the number of experimental points. As a starting point for the WS potential, we have used the potential of Akyuz-Winther [35]. The resulting optical parameters are specified in Table I, while in Fig. 1 the real parts of the optical potentials and the OM calculation results are shown.

From Fig. 1(a), we see that different depths are obtained in the calculated potentials. In particular, the WS potential shows a remarkable lower depth. However, all three potentials show a similar decreasing tendency in the tails meaning that the nuclear reaction bears more surface character. The M3Y-ZR and DDM3Y-FR potentials are close to each other and have indistinguishable shapes starting from 5 fm. It is worth noting that the knock-on exchange and density dependence effects included in DDM3Y-FR makes it less deeper with respect to M3Y-ZR.

Both real and imaginary volume integrals for nucleon pairs of WS potential turned out to be phenomenally low when compared to other two potentials (see Table I). This behavior is not surprising, taking into account well-known ambiguities of the WS potentials [36,37]. Instead, the calculated volume integrals per nucleon pairs J_{Re} for M3Y-ZR and DDM3Y-FR are not much different from those appearing in the studies carried out in Refs. [24,27,38,39].

The total cross sections, σ_r, were also obtained for the used optical potentials, and the results are given in Table I. The reaction cross section for the phenomenological potential WS is found to be about 17% lower than the cross sections obtained with other two semimicroscopic potentials. It is interesting to note that a similar study, but on the interaction of the oxygen isotope ^{16}O with ^{40}Ca at 214 MeV beam energy, also observed an analogous tendency [40]. Moreover, our calculated reaction cross sections for the M3Y-ZR and DDM3Y-FR potentials are well consistent with those results obtained in Ref. [40].

B. Inelastic channel

The coupling potential has been built within the perturbation theory by deforming the spherical interaction potential $U(R)$ to a slightly axially deformed shape, characterized by the length δ_λ. The radial dependence of the coupling potential then becomes

$$V_{ii'}^\lambda(R) = -\frac{\delta_\lambda^{i \to i'}}{4\pi} \frac{dU(R)}{dR}, \quad (7)$$

where i and i' are the elastic and inelastic channels, respectively.

We have used the FRESCO code [21] to reproduce the cross sections of inelastic angular distributions by employing the optical potentials obtained from the OM analysis. The experimental angular distributions are compared with the calculated results for the three potentials in Fig. 2. A good reproduction of experimental data is obtained with the DDM3Y-FR and M3Y-ZR. The double folding potentials fairly catch the absolute cross section and the oscillation pattern of the data.

The analysis helped us to extract the quadrupole deformation parameter β_2 for the transition $0^+ \to 2^+$ in the oxygen isotope, which is related to the deformation length as $\beta_2 = \delta_2 R_{int}^{-1}$ with R_{int} standing for the interaction radius. Thus, the obtained quadrupole deformation parameter turned out to be $\beta_2 = 0.2 \pm 0.01$, which is quite similar to that parameter $\beta_2 = 0.216$ obtained in the analysis of the ^{18}O + ^{74}Ge inelastic scattering [41]. In addition, in terms of the deformation
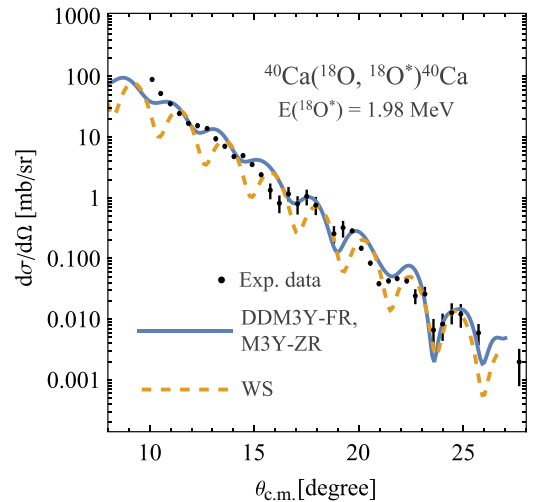
FIG. 2. Angular distributions of inelastic scattering in comparison with the theoretical estimations with the different potentials. Experimental data are taken from Ref. [24].
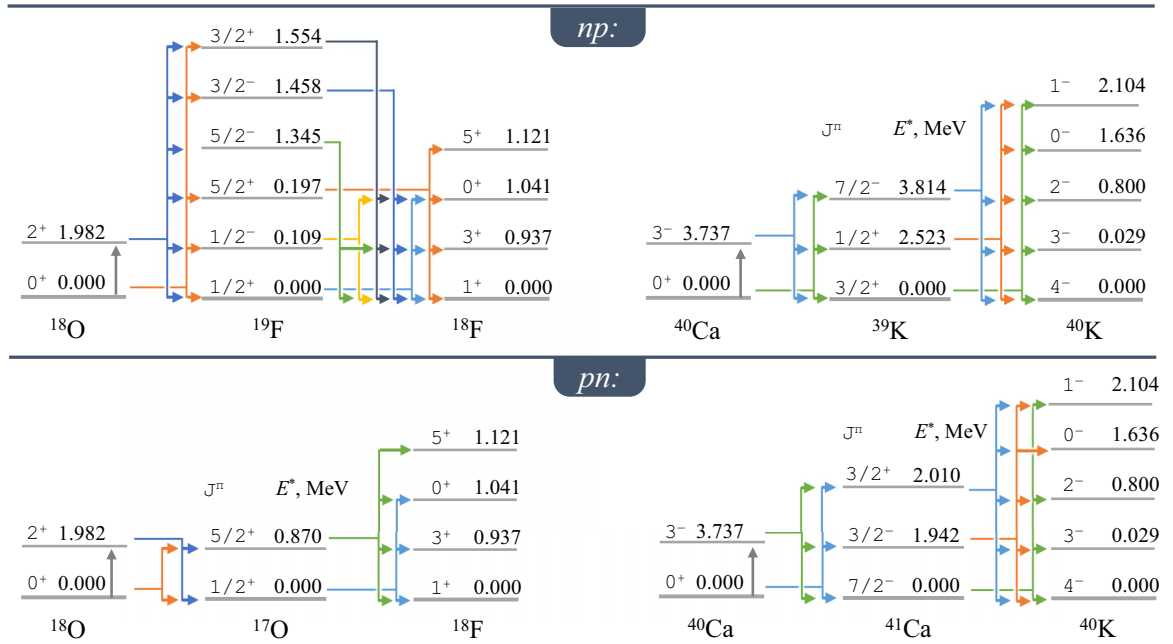
FIG. 3. Coupling schemes used in the inelastic, one-nucleon and two-step transfer DWBA calculations. Left side is for projectile overlaps, while right side is for target overlaps.

lengths, our obtained value $\delta_2 = 1.19$ fm is in good accordance with the result $\delta_2 = 1.15$ fm deduced with the reaction $^{18}O + ^{12}C$ [42].

III. NEUTRON STRIPPING AND PROTON PICK-UP CHANNELS

Both neutron stripping and proton pick-up channels have been studied within the DWBA method. The arrangement of the channel couplings is shown in Fig. 3. For the entrance channel, we have adopted the DDM3Y-FR potential, constrained to produce the elastic and inelastic scattering cross sections as described above. In the exit channels we utilized the same semimicroscopic potential as in the entrance channel, since the nuclear density distribution functions of both projectile and projectile-like nuclei (or target and target-like nuclei) obtained within the HFB method are quite similar. The transition amplitude was taken in the *prior* form with the complex remnant term. As regards the radial wave functions for the bound states, they were designed in order to reproduce the binding energies by means of the well-depth procedure with the WS potential. In this case, the radius and diffuseness parameters of the potential were fixed as 1.25 fm and 0.65 fm, respectively.

The one-particle spectroscopic amplitudes, A_{lsj}^{jIJ}, were obtained through the use of the KSHELL code [43]. For projectile overlaps, the amplitudes were calculated in the *p-sd* model space by implementing the YSOXT effective interaction from Ref. [44], for the target overlaps, we have adopted the SDPF−mu effective interaction on the *sd-pf* model space taken from [45]. The calculated *n*-stripping and *p*-pick-up spectroscopic amplitudes are given in Table II.

In Fig. 4(a), the angular distributions on the *n*-stripping reactions obtained by DWBA calculations are presented. The theoretical results reproduce the experimental data as well as those reported in Ref. [26]. The spectroscopic amplitudes used in the current work turned out to be, in fact, similar to those calculated by Calabrese *et al.* [26].

Another DWBA analysis for the reaction (d, p) on the target ^{40}Ca [46] showed approximately the same information as that predicted by our shell-model calculations. In particular, the analyses in Ref. [46] revealed that the spectroscopic factor varies from 0.95 to 1.14 depending on the projectile energy for the overlap $\langle ^{41}Ca, \frac{7}{2}_1^- ||0f_{7/2}|| ^{40}Ca, 0_1^+ \rangle$. While, in the current study the amplitude is +0.99 (see Table II) (generating spectroscopic factor 0.98), which fits well with the (d, p) reaction study.

Figures 4(b)–4(d) illustrates the results of calculations for the *p*-pick-up transfer reactions. In this figure, angular distributions for the most probable transitions are sketched. It is interesting to note that in Fig. 4(b) the total angular distribution is dominated by $^{19}F_{0.197} + ^{39}K_{gs}$ rather than the $^{19}F_{gs} + ^{39}K_{gs}$ exit channel. The predominance of $^{19}F_{0.197}$ compared to the transition $^{19}F_{gs}$ in the proton transfer is also observed for other excited state of ^{41}Ca [see Figs. 4(b) and 4(d)] and has been reported in several studies on different targets [26,42,47,48]. This is attributed to the larger amplitude (0.67, see Table II) for the transition from $^{18}O_{gs}$ to $^{19}F_{0.197}$, respect to the ground state ^{19}F (0.58, see Table II).

It is also interesting to note that our calculated spectroscopic amplitudes for the overlaps $\langle ^{40}Ca, 0_1^+ ||0d_{3/2}|| ^{39}K, \frac{3}{2}_1^+ \rangle$ and $\langle ^{40}Ca, 0_1^+ ||1s_{1/2}|| ^{39}K, \frac{1}{2}_1^+ \rangle$ are comparable with those obtained by means of the the source-term approach for one doubly closed-shell nuclei [49]. In particular, for population of proton in $0d_{3/2}$, the author obtained the spectroscopic factor

TABLE II. Spectroscopic amplitudes used in the DWBA calculations for n-stripping and p-pick-up reactions. The amplitudes correspond to the coupling order as Composite (A) = Core (A − 1) + N system.

A	J^π	E^*_A [MeV]	A − 1	I^π	E^*_{A-1} [MeV]	n	l	j	A^{jIJ}_{lsj}
^{19}F	$1/2^-$	0.109	^{18}O	0^+	0.0	0	1	1/2	0.1176
				2^+	1.982	0	1	3/2	0.0137
	$1/2^+$	0.0		0^+	0.0	1	0	1/2	−0.5761
				2^+	1.982	0	2	3/2	−0.3003
						0	2	5/2	0.6059
	$3/2^-$	1.458		0^+	0.0	0	1	3/2	0.0073
				2^+	1.982	0	1	1/2	−0.0996
						0	1	3/2	−0.0004
	$3/2^+$	1.554		0^+	0.0	0	2	3/2	−0.4605
				2^+	1.982	0	2	3/2	0.3335
						0	2	5/2	0.2944
						1	0	1/2	0.4001
	$5/2^-$	1.345		2^+	1.982	0	1	1/2	0.0891
						0	1	3/2	0.0008
	$5/2^+$	0.197		0^+	0.0	0	2	5/2	0.6693
				2^+	1.982	0	2	3/2	0.1607
						0	2	5/2	−0.4324
						1	0	1/2	−0.3602
^{40}Ca	0^+	0.0	^{39}K	$1/2^+$	2.523	1	0	1/2	−1.3878
				$3/2^+$	1.942	0	2	3/2	−1.9569
				$7/2^-$	0.0	0	3	7/2	0.2063
	3^-	3.737		$1/2^+$	2.523	0	3	7/2	−0.3932
						0	3	5/2	−0.1786
				$3/2^+$	1.942	0	3	7/2	0.3676
^{40}Ca	3^-	3.737	^{39}K	$3/2^+$	0.0	0	3	5/2	−0.1849
						1	1	3/2	0.2501
				$7/2^-$	3.814	0	2	5/2	0.0447
						0	2	3/2	−0.6616
						1	0	1/2	−0.0093
^{18}O	0^+	0.0	^{17}O	$1/2^+$	0.0	1	0	1/2	0.3545
				$5/2^+$	0.870	0	2	5/2	−0.5203
	2^+	1.982		$1/2^+$	0.0	0	2	3/2	−0.1991
						0	2	5/2	−0.2242
				$5/2^+$	0.870	0	2	3/2	0.0546
						0	2	5/2	0.466
						1	0	1/2	0.502
^{41}Ca	$3/2^-$	1.942	^{40}Ca	0^+	0.0	1	1	3/2	0.9932
				3^-	3.737	0	2	5/2	−0.0663
						0	2	3/2	0.2452
	$3/2^+$	2.010		0^+	0.0	0	2	3/2	−0.0989
				3^-	3.737	0	3	7/2	−0.1355
						0	3	5/2	0.0626
						1	1	3/2	0.0467
	$7/2^-$	0.0		0^+	0.0	0	3	7/2	0.9864
				3^-	3.737	0	2	5/2	−0.1124
						0	2	3/2	0.2775
						1	0	1/2	−0.3658

2.63 in contrast with the calculated one in this work 3.84 (generated with the amplitude −1.96, see Table II). As regards $0s_{1/2}$, in that work the spectroscopic factor is given as 1.05, while the same factor in this work is 1.93 (generated by the amplitude −1.39, see Table II). A slight difference in spectroscopic factors can be caused by the effect of 3N interaction taken into account within the source-term approach. Indeed, we should note that the 3N interactions were not presented in the shell model calculations in the current work.

IV. TWO-STEP TRANSFER MECHANISMS

The two-step transfer mechanisms were calculated within the N-step DWBA approach. Coupled equations were iterated two times in order to get distorted wave functions of the final channels. The nonorthogonal terms were avoided in the calculations by choosing the *prior* form in the first DWBA transition and the *post* form in the second transition [27]. The same optical potential, constrained by elastic, inelastic, one-nucleon transfer channels was adopted in the two-step transfer calculations. Due to the similarities of the nuclear densities of nuclei in the entrance and exit channels, the semimicroscopic folding potential was also applied as the nuclear parts of exit channels. The spectroscopic amplitudes were calculated in the same way as it was done in the previous section. The results of the shell-model calculations used in the DWBA calculations of the second step are presented in Table III.

In order to account for the two indistinguishable quantum routes feeding single charge exchange process, the correct description of the experimental angular distribution data for the channel i requires model calculations arranged as follows:

$$\frac{\mathrm{d}\sigma}{\mathrm{d}\Omega}(\theta)_i = |f_i^{np}(\theta) + f_i^{pn}(\theta)|^2. \tag{8}$$

Here, $f_i^{np}(\theta)$ and $f_i^{pn}(\theta)$ are the transition amplitudes for the transfer mechanisms of np and pn, respectively.

In addition, to describe the experimental spectral shapes analyzed in the experiment, one should consider that not always individual transitions are isolated, being instead integrated all together within a region of interest. Thus all the transition cross sections in the same region of interest (RoI) are summed up incoherently:

$$\frac{\mathrm{d}\sigma}{\mathrm{d}\Omega}(\theta)_k = \sum_i \frac{\mathrm{d}\sigma}{\mathrm{d}\Omega}(\theta)_i, \tag{9}$$

where k indicates the specific region of interest.

Based on the two-step transfer mechanisms, the DWBA calculation results are illustrated in Fig. 5 with the the same resolution and scale. The most contributory channels are exactly named in the caption. In this figure, we present only the channels where contributions are non-negligible or larger than 10^{-4} mb/sr. In the first RoI $k(1)$ it is seen that the channel ^{18}F$_{gs}$ + ^{40}K$_{0.03}$ prevails over the channel in the ground state of ^{40}K. Interestingly, the opposite trend was reported in the study in the meson-exchange one-step QRPA framework [24]. It is
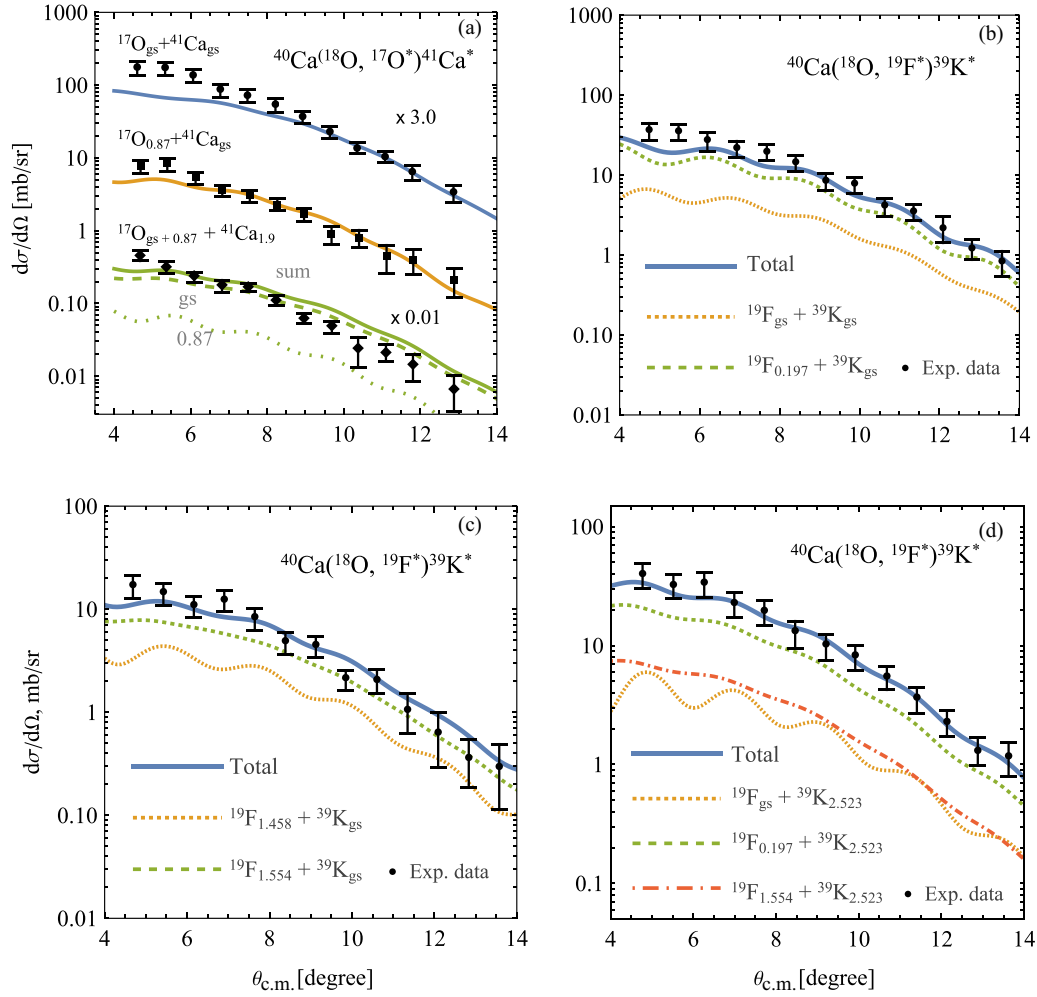
FIG. 4. DWBA calculation results for the neutron stripping (a) and proton pick-up (b)–(d) channels in comparison with the experimental cross sections for various excited states of colliding nuclei. Experimental data are taken from [26].
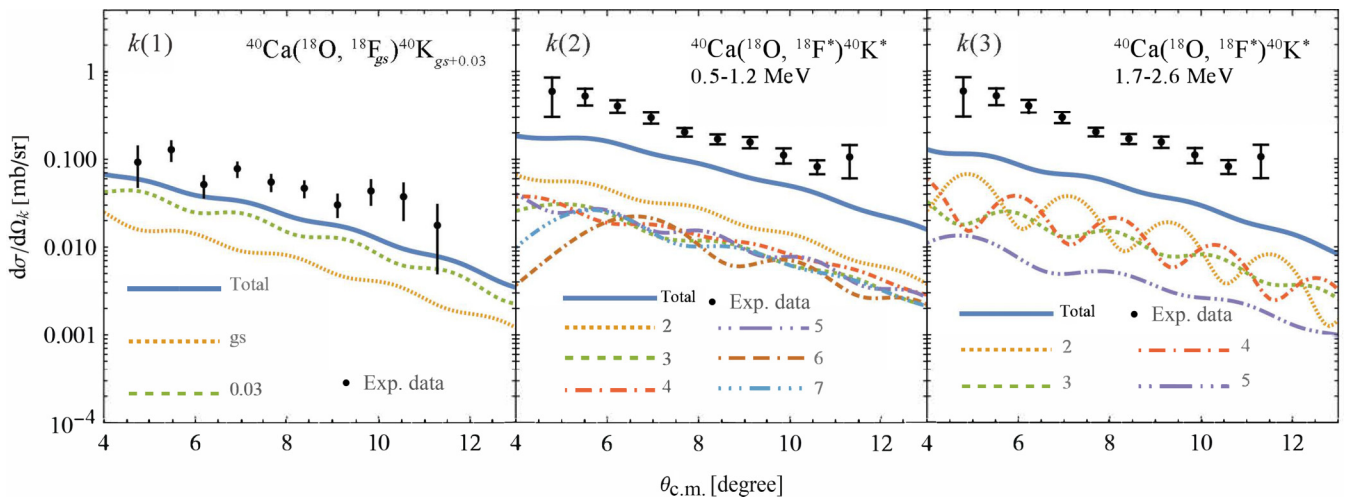
FIG. 5. DWBA calculation results of the two-step transfer mechanisms in comparison with the differential cross sections according to the experimental regions of interest (RoI). $k(1) - {}^{18}F_{gs} + {}^{40}K_{gs+0.03}$ experimental data and corresponding DWBA to the curves: Total, ${}^{18}F_{gs} + {}^{40}K_{gs}$, ${}^{18}F_{gs} + {}^{40}K_{0.03}$; $k(2) - $ the experimental RoI between 0.5–1.2 MeV and corresponding DWBA to the curves: Total, 2: ${}^{18}F_{gs} + {}^{40}K_{0.8}$, 3: ${}^{18}F_{0.937} + {}^{40}K_{gs}$, 4: ${}^{18}F_{0.937} + {}^{40}K_{0.03}$, 5: ${}^{18}F_{1.042} + {}^{40}K_{0.03}$, 6: ${}^{18}F_{1.121} + {}^{40}K_{gs}$, 7: ${}^{18}F_{1.121} + {}^{40}K_{0.03}$; $k(3) - $ the experimental RoI between 1.7–2.6 MeV and corresponding DWBA to the curves. Total, 2: ${}^{18}F_{gs} + {}^{40}K_{2.1}$, 3: ${}^{18}F_{0.937} + {}^{40}K_{2.1}$, 4: ${}^{18}F_{1.041} + {}^{40}K_{2.1}$, 5: ${}^{18}F_{1.121} + {}^{40}K_{2.1}$. Experimental data are taken from [24].

TABLE III. Spectroscopic amplitudes used in the second step of DWBA calculations for np and pn reaction mechanisms. The amplitudes correspond to the coupling order as Composite (A) = Core (A − 1) + N system.

A	J^π	E^*_A [MeV]	A − 1	I^π	E^*_{A-1} [MeV]	n	l	j	A^{jIJ}_{lsj}
^{19}F	$1/2^-$	0.109	^{18}F	0^+	1.041	0	1	1/2	0.1326
				1^+	0.0	0	1	1/2	−0.0206
						0	1	3/2	−0.1623
	$1/2^+$	0.0		0^+	1.041	1	0	1/2	−0.3989
				1^+	0.0	0	2	3/2	−0.0059
						1	0	1/2	−0.7335
				3^+	0.937	0	2	5/2	−0.7799
	$3/2^-$	1.458		0^+	1.041	0	1	3/2	0.0118
				1^+	0.0	0	1	1/2	0.0631
						0	1	3/2	−0.0198
				3^+	0.937	0	1	3/2	−0.1145
	$3/2^+$	1.554		0^+	1.041	0	2	3/2	−0.3179
				1^+	0.0	0	2	3/2	0.1838
						0	2	5/2	0.8656
				1^+	0.0	1	0	1/2	0.0178
				3^+	0.937	0	2	3/2	0.1793
						0	2	5/2	0.299
	$5/2^-$	1.345		1^+	0.0	0	1	3/2	0.0246
				3^+	0.937	0	1	1/2	0.0098
						0	1	3/2	0.0755
	$5/2^+$	0.197		0^+	1.041	0	2	5/2	0.4619
				5^+	1.121	0	2	5/2	0.6684
				1^+	0.0	0	2	3/2	0.2934
						0	2	5/2	0.5513
				3^+	0.937	0	2	3/2	0.1042
						0	2	5/2	0.4734
						1	0	1/2	0.4432
^{40}K	0^-	1.636	^{39}K	$1/2^+$	2.523	1	1	1/2	−0.1453
				$3/2^+$	0.0	1	1	3/2	−0.9809
	1^-	2.104		$1/2^+$	2.523	1	1	3/2	0.0183
						1	1	1/2	−0.019
				$3/2^+$	0.0	0	3	5/2	0.0461
						1	1	3/2	−0.9448
						1	1	1/2	−0.2855
				$7/2^-$	3.814	0	2	5/2	0.0543
	2^-	0.8		$1/2^+$	2.523	0	3	5/2	−0.0321
						1	1	3/2	0.1552
				$3/2^+$	0.0	0	3	7/2	−0.9559
						0	3	5/2	−0.0436
						1	1	3/2	0.1093
						1	1	1/2	0.0368
				$7/2^-$	3.814	0	2	5/2	0.1053
						0	2	3/2	−0.4552
	3^-	0.029		$1/2^+$	2.523	0	3	7/2	−0.1988
						0	3	5/2	0.0275
				$3/2^+$	0.0	0	3	7/2	−0.9524
						0	3	5/2	−0.0266
						1	1	3/2	0.1401
				$7/2^-$	3.814	0	2	5/2	0.0241
						0	2	3/2	0.1528

A	J^π	E^*_A [MeV]	A − 1	I^π	E^*_{A-1} [MeV]	n	l	j	A^{jIJ}_{lsj}
^{40}K	3^-	0.029	^{39}K	$7/2^-$	3.814	1	0	1/2	0.0454
	4^-	0.0		$1/2^+$	2.523	0	3	7/2	−0.1355
				$3/2^+$	0.0	0	3	7/2	0.9735
						0	3	5/2	−0.035
				$7/2^-$	3.814	0	2	5/2	−0.1
						0	2	3/2	0.2701
						1	0	1/2	−0.2027
^{18}F	0^+	1.041	^{17}O	$1/2^+$	0.0	1	0	1/2	−0.3617
				$5/2^+$	0.870	0	2	5/2	−0.8938
	5^+	1.121				0	2	5/2	−0.9815
	1^+	0.0		$1/2^+$	0.0	0	2	3/2	0.154
						1	0	1/2	−0.5099
				$5/2^+$	0.870	0	2	3/2	0.4747
						0	2	5/2	−0.471
	3^+	0.937		$1/2^+$	0.0	0	2	5/2	−0.5487
				$5/2^+$	0.870	0	2	3/2	0.1653
						0	2	5/2	−0.54
						1	0	1/2	−0.5513
^{41}Ca	$3/2^-$	1.942	^{40}K	0^-	1.636	0	2	3/2	0.4831
				1^-	2.104	0	2	5/2	−0.0486
						0	2	3/2	0.8059
						1	0	1/2	−0.0153
				2^-	0.8	0	2	5/2	−0.0001
						0	2	3/2	−0.1201
						1	0	1/2	−0.1709
				3^-	0.029	0	2	5/2	−0.0054
						0	2	3/2	−0.1823
				4^-	0.0	0	2	5/2	−0.0029
	$3/2^+$	2.010		0^-	1.636	1	1	3/2	0.0404
				1^-	2.104	0	3	5/2	−0.0246
						1	1	3/2	−0.0351
						1	1	1/2	0.0129
				2^-	0.8	0	3	7/2	0.3557
						0	3	5/2	−0.0013
						1	1	3/2	0.0926
				2^-	0.8	1	1	1/2	−0.0314
				3^-	0.029	0	3	7/2	−0.1855
						0	3	5/2	0.0884
						1	1	3/2	−0.0469
				4^-	0.0	0	3	7/2	−0.23
						0	3	5/2	0.1345
	$7/2^-$	0.0		1^-	2.104	0	2	5/2	0.0448
				2^-	0.8	0	2	5/2	−0.112
						0	2	3/2	0.75
				3^-	0.029	0	2	5/2	0.041
						0	2	3/2	0.8837
						1	0	1/2	0.1852
				4^-	0.0	0	2	5/2	0.0401
						0	2	3/2	−1.0243
						1	0	1/2	0.1431

worth noting that the shape of the cross section of the exit channel with ^{40}K resembles the one that was calculated also within the QRPA maybe due to the common distortion effect of the optical potential. The absolute values of one- (from Ref. [24]) and our two-step SCE also compete, thus suggesting a sizable interference among them in the measured cross sections. We can thus conclude that *i*) an accurate treatment of two-step mechanisms cannot be omitted and *ii*) a further step is to incorporate one- and two-step mechanisms in the same consistent calculation, which is a highly desirable although non trivial development.

In the RoI $k(2)$, all six channels have similar contribution, except the most dominant channel $^{18}F_{gs} + {}^{40}K_{0.8}$. Nevertheless, the sum of DWBA cross sections underestimates the experimental points. The comparison becomes worse in the RoI $k(3)$. It can be interpreted as the domination of the direct charge exchange mechanisms. Such a kind of picture coincides with the finding reported in the study [24], where it is shown that the higher excitation in the exit channels, the greater the contribution due to the meson exchange process.

Similar trends were found in Refs. [4,50,51]. The SCE reaction $^{26}Mg(^{12}C, {}^{12}B)^{12}Al^*$ at the laboratory energy of 102 MeV is studied in Ref. [50]. With the ground state in the exit channel, the direct method of calculations was factorized up to 2 orders of magnitude depending on the interaction type, whereas in the two-step transfer mechanisms the factorisation was close to unity. In the work [51], the reaction $^{12}C(^7Li, {}^7Be)^{12}B$ was studied at the laboratory energy of 82 MeV. The SCE and two-step mechanisms were analyzed within the DWBA method with the modelled form factors. The authors stated that two-step transfer mechanisms play a dominant role in the reaction. Moreover, the list of normalisation factors was tabled depending on the excited states of ^{12}B. It can be seen that the higher excitation of ^{12}B, the stronger the SCE contribution.

It is interesting to see how a pair of nucleons is transferred in the SCE reaction channels. Figure 6 presents the differential sections for this reaction regarding the competition of reaction mechanisms. For the exit channel $^{18}F + {}^{40}K_{gs}$, it is observed that the mechanisms *np* and *pn* compete with each other with a slight predominance of the mechanisms *pn*.

V. CONCLUSIONS

In this work, a wide set of direct reactions stemming from the $^{18}O + {}^{40}Ca$ collision at an energy of 275 MeV was consistently studied. The differential cross section for elastic scattering was obtained within the optical model, while the inelastic, one-nucleon, two-step transfer channels were calculated by employing the DWBA method. The calculated semimicroscopic potentials, DDM3Y-FR and M3Y-ZR, were obtained within the double folding model. The double folding potentials, which notoriously give a transparent average description of the nucleus nucleus interaction, were found to be much better in describing elastic and inelastic cross section data than the WS phenomenological potential. The deformation length for the transition $0^+ \rightarrow 2^+$ in ^{18}O was extracted from the inelastic scattering analysis. The deformation length is 1.19 fm, and it is well consistent with the
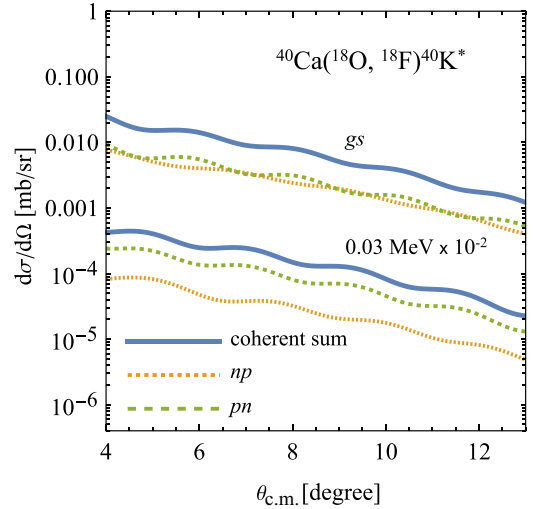
FIG. 6. DWBA calculation results in terms of *np* and *pn* transfer mechanisms for the SCE channels at the ground and excited (0.03 MeV) states of ^{40}K.

previous studies. Based on this view, the double folding potential DDM3Y-FR was applied to DWBA calculations for one- and two-nucleon transfer cross sections, the latter specifically connected to the SCE process. The calculated spectroscopic data using the YSOXT effective nucleon-nucleon potentials for *p-sd* and the SDPF-mu potential in the *sd-pf* mixed shells turned out to be similar those of the other studies [42,46,49].

The focus was on the two-step transfer mechanisms in the reaction $^{40}Ca(^{18}O, {}^{18}F)^{40}K$. In fact, it has been found that compared to the results of DWBA calculations assuming meson exchange microscopic form factors derived by QRPA approaches [24], the two-step transfer mechanisms, *np* and *pn*, have a comparable relevance. Interestingly, the present study corroborates the conclusion of Ref. [24] of the complementary contribution of both one- and two-step processes in SCE reaction, at least at the experimental conditions examined here. In particular, the one-step meson exchange process has an increasing role as the excitation energy of the system rises. This points to the need of a complete calculation for single charge exchange cross section, where the reaction model space accommodates both one- and two-step routes with consistent inputs from nuclear structure model, either shell model or QRPA or other. Such a research program is, in our opinion the main development we suggest in the field and we are committed alongside to reach this milestone. A decreasing in the dynamics of the contribution of *np* and *pn* to the cross sections depending on the excitation energy of $^{18}F^*$ and $^{40}K^*$ was also confirmed.

[1] Y. Fujita, H. Akimune, I. Daito, M. Fujiwara, M. N. Harakeh, T. Inomata, J. Jänecke, K. Katori, C. Lüttge, S. Nakayama, P. von Neumann-Cosel, A. Richter, A. Tamii, M. Tanaka, H. Toyokawa, H. Ueno, and M. Yosoi, Phys. Rev. C **55**, 1137 (1997).

[2] H. Ejiri, Phys. Rep. **338**, 265 (2000).

[3] Y. Fujita, B. Rubio, and W. Gelletly, Prog. Part. Nucl. Phys. **66**, 549 (2011).

[4] M. C. Etchegoyen, A. Etchegoyen, B. H. Wildenthal, B. A. Brown, and J. Keinonen, Phys. Rev. C **38**, 1382 (1988).

[5] B. M. Loc, N. Auerbach, and D. T. Khoa, Phys. Rev. C **96**, 014311 (2017).

[6] J. J. Li, C. A. Bertulani, Y. Liu, J. L. Lou, D. Y. Pang, X. H. Sun, B. Yang, X. F. Yang, and Y. L. Ye, Phys. Rev. C **102**, 064601 (2020).

[7] D. Frekers and M. Alanssari, Eur. Phys. J. A **54**, 177 (2018).

[8] B. V. Danilin, M. V. Zhukov, S. N. Ershov, F. A. Gareev, R. S. Kurmanov, J. S. Vaagen, and J. M. Bang, Phys. Rev. C **43**, 2835 (1991).

[9] K. Yako, H. Sakai, M. B. Greenfield, K. Hatanaka, M. Hatano, J. Kamiya, H. Kato, Y. Kitamura, Y. Maeda, C. L. Morris *et al.*, Phys. Lett. B **615**, 193 (2005).

[10] F. Cappuzzello, C. Agodi, M. Cavallaro, D. Carbone, S. Tudisco, D. Lo Presti, J. Oliveira, P. Finocchiaro, M. Colonna, D. Rifuggiato *et al.*, Eur. Phys. J. A **54**, 72 (2018).

[11] H. Lenske, F. Cappuzzello, M. Cavallaro, and M. Colonna, Prog. Part. Nucl. Phys. **109**, 103716 (2019).

[12] F. Cappuzzello, H. Lenske, M. Cavallaro, C. Agodi, N. Auerbach, J. Bellone, R. Bijker, S. Burrello, S. Calabrese, D. Carbone *et al.*, Prog. Part. Nucl. Phys. **128**, 103999 (2023).

[13] N. Shimizu, J. Menéndez, and K. Yako, Phys. Rev. Lett. **120**, 142502 (2018).

[14] J. Menéndez, N. Shimizu, and K. Yako, J. Phys.: Conf. Ser. **1056**, 012037 (2018).

[15] F. Cappuzzello, M. Cavallaro, C. Agodi, M. Bondì, D. Carbone, A. Cunsolo, and A. Foti, Eur. Phys. J. A **51**, 145 (2015).

[16] J. I. Bellone, S. Burrello, M. Colonna, J.-A. Lay, and H. Lenske (NUMEN Collaboration), Phys. Lett. B **807**, 135528 (2020).

[17] H. Lenske, J, Phys.: Conf. Ser. **1056**, 012030 (2018).

[18] E. Santopinto, H. García-Tecocoatzi, R. I. M. Vsevolodovna, and J. Ferretti (NUMEN Collaboration), Phys. Rev. C **98**, 061601(R) (2018).

[19] J. L. Ferreira, J. Lubian, F. Cappuzzello, M. Cavallaro, and D. Carbone (NUMEN Collaboration), Phys. Rev. C **105**, 014630 (2022).

[20] C. Brendel, P. von Neumann-Cosel, A. Richter, G. Schrieder, H. Lenske, H. Wolter, J. Carter, and D. Schüll, Nucl. Phys. A **477**, 162 (1988).

[21] I. J. Thompson, Comput. Phys. Rep. **7**, 167 (1988).

[22] H. Lenske, H. H. Wolter, and H. G. Bohlen, Phys. Rev. Lett. **62**, 1457 (1989).

[23] F. Cappuzzello, H. Lenske, A. Cunsolo, D. Beaumel, S. Fortier, A. Foti, A. Lazzaro, C. Nociforo, S. Orrigo, and J. Winfield, Nucl. Phys. A **739**, 30 (2004).

[24] M. Cavallaro, J. I. Bellone, S. Calabrese, C. Agodi, S. Burrello, F. Cappuzzello, D. Carbone, M. Colonna, N. Deshmukh, H. Lenske *et al.*, Front. Astron. Space Sci. **8**, 659815 (2021).

[25] H. Lenske, J. I. Bellone, M. Colonna, J.-A. Lay *et al.* (NUMEN Collaboration), Phys. Rev. C **98**, 044620 (2018).

[26] S. Calabrese *et al.* (NUMEN Collaboration), Phys. Rev. C **104**, 064609 (2021).

[27] G. R. Satchler, *Direct Nuclear Reactions* (Clarendon, Press, Oxford, 1983).

[28] R. V. Reid, Ann. Phys. **50**, 411 (1968).

[29] D. T. Khoa and W. von Oertzen, Phys. Lett. B **342**, 6 (1995).

[30] M.-E. Brandan and G. R. Satchler, Phys. Rep. **285**, 143 (1997).

[31] M. Karakoç, Comput. Phys. Commun. **284**, 108613 (2023).

[32] S. Goriely, M. Samyn, and J. M. Pearson, Phys. Rev. C **75**, 064312 (2007).

[33] I. Angeli, At. Data Nucl. Data Tables **87**, 185 (2004).

[34] G. Audi, A. Wapstra, and C. Thibault, Nucl. Phys. A **729**, 337 (2003).

[35] O. Akyuz and A. Winther, in *Proceedings of the Enrico Fermi School of Physics, 1979*, edited by R. A. Broglia, C. H. Dasso, and R. Ricci, Course on Nuclear Structure and Heavy-Ion Reactions (North-Holland, Amsterdam, 1981), p. 491.

[36] G. R. Satchler and W. G. Love, Phys. Rep. **55**, 183 (1979).

[37] H.-J. Trost, A. Schwarz, U. Feindt, F. Heimlich, S. Heinzel, J. Hintze, F. Körber, R. Lekebusch, P. Lezoch, G. Möck *et al.*, Nucl. Phys. A **337**, 377 (1980).

[38] L. Gan, Z.-H. Li, H.-B. Sun, S.-P. Hu, E.-T. Li, and J. Zhong, Chin. Phys. C **45**, 054105 (2021).

[39] L. La Fauci *et al.* (NUMEN collaboration), Phys. Rev. C **104**, 054610 (2021).

[40] M. Hassanain, H. Alshrani, A. A. Ibraheem, M. Anwar, K. O. Behairy, Z. M. Mahmoud, and E. M. Darwish, Phys. At. Nucl. **82**, 615 (2019).

[41] M.-C. Lemaire and K. S. Low, Phys. Rev. C **16**, 183 (1977).

[42] A. Spatafora *et al.* (NUMEN Collaboration), Phys. Rev. C **107**, 024605 (2023).

[43] N. Shimizu, T. Mizusaki, Y. Utsuno, and Y. Tsunoda, Comput. Phys. Commun. **244**, 372 (2019).

[44] C. Yuan, T. Suzuki, T. Otsuka, F. Xu, and N. Tsunoda, Phys. Rev. C **85**, 064324 (2012).

[45] Y. Utsuno, T. Otsuka, B. A. Brown, M. Honma, T. Mizusaki, and N. Shimizu, Phys. Rev. C **86**, 051301(R) (2012).

[46] D. Kocher and W. Haeberli, Nucl. Phys. A **172**, 652 (1971).

[47] L. Green, C. Lennon, and I. Naqib, Nucl. Phys. A **142**, 137 (1970).

[48] O. Sgouros *et al.* (for the NUMEN Collaboration), Phys. Rev. C **104**, 034617 (2021).

[49] N. Timofeyuk, J. Phys. G: Nucl. Part. Phys. **48**, 015105 (2020).

[50] A. Etchegoyen, D. Sinclair, S. Liu, M. Etchegoyen, D. Scott, and D. Hendrie, Nucl. Phys. A **397**, 343 (1983).

[51] S. Sakuta, Y. A. Glukhov, A. Rudchik, V. M. Pirnak, V. Ziman, A. Budzanowski, S. Kliczewski, R. Siudak, I. Skwirczyńska, and A. Szczurek, Nucl. Phys. A **773**, 187 (2006).